Chapter 8

Widely Tunable Quantum-Dot Source Around 3 μm

Alice Bernard, Marco Ravaro, Jean-Michel Gerard, Michel Krakowski, Olivier Parillaud, Bruno Gérard, Ivan Favero and Giuseppe Leo

Additional information is available at the end of the chapter

http://dx.doi.org/10.5772/intechopen.70753

Abstract

We propose a widely tunable parametric source in the 3 μm range, based on intracavity spontaneous parametric down conversion (SPDC) of a quantum-dot (QD) laser emitting at 1.55 μm into signal and idler modes around 3.11 μm. To compensate for material dispersion, we engineer the laser structure to emit in a higher-order transverse mode of the waveguide. The width of the latter is used as a degree of freedom to reach phase matching in narrow, deeply etched ridges, where the in-plane confinement of the QDs avoids non-radiative sidewall electron-hole recombination. Since this design depends critically on the knowledge of the refractive index of $In_{1-x}Ga_xAs_yP_{1-y}$ lattice matched to InP at wavelengths where no data are available in the literature, we have accurately determined them as a function of wavelength (λ = 1.55, 2.12 and 3 μm) and arsenic molar fraction (y = 0.55, 0.7 and 0.72) with a precision of $\pm 4 \times 10^{-3}$. A pair of dichroic dielectric mirrors on the waveguide facets is shown to result in a continuous-wave optical parametric oscillator (OPO), with a threshold around 60 mW. Emission is tunable over hundreds of nanometers and expected to achieve mW levels.

Keywords: quantum dots, laser diode, near infrared, InGaAsP, tunable source, OPO

1. Introduction

The tunability of currently available integrated sources is limited to a few tens of nanometers at most, via temperature or current control. While this is not a problem for most applications, certain fields like wavelength division multiplexing and spectroscopy are in demand of sources with broader tunability and choice of spectral range. Spectroscopy, especially, requires wide-band, continuously tunable sources with narrow emission lines. The 2–4 μm wavelength interval

is of particular interest since it contains various peaks of atmospheric and hydrocarbon molecules, with important applications in environmental monitoring, security, and medicine [1–4]. This spectral region is at the frontier between the emission ranges of diodes and quantum cascade lasers (QCLs), and to date most existing sources around 3 μm, such as short-wavelength QCLs [5, 6] or GaSb diodes [7], are only available in laboratories. Interband cascade lasers (ICLs) are the only sources commercially available in this wavelength range, albeit at a high price [8–10]. Moreover, the tunability range of all these devices is limited to a few tens of nanometers. As a consequence, individual laser diodes are used for each spectroscopic line of absorption, which increases the price of a complete diagnosis based on several lines. In this context, nonlinear optics offers a solution for widely wavelength tunable sources, bulky tabletop optical parametric oscillators (OPOs) being commonly used to provide high-quality, tunable beams. Most miniaturized OPOs have been demonstrated in $LiNbO_3$ [11, 12], but an OPO threshold has been achieved in a GaAs micrometric waveguide [13] with a potential span of 500 nm. Like GaAs, InP is an attractive material for its high $\chi^{(2)}$ and mature technology, especially for emission at 1.55 μm.

Here we report on the design of an InGaAsP/InP QD laser diode emitting at 1.55 μm, optimized for intracavity spontaneous parametric down conversion (SPDC) around 3.11 μm via modal phase matching. The use of QDs is justified by the choice of narrow, deeply etched structures insofar they have been shown to trap carriers and limit surface recombination [14], and narrow-ridge, low-threshold InAs/InP QD lasers have already been demonstrated [15]. In order to estimate the phase mismatch accurately, a precise knowledge of the refractive indices is critical at pump, signal, and idler wavelengths. While the index of InGaAsP lattice matched to InP is well known at 1.55 μm [16–20], to date only one publication deals with its measurement at longer wavelengths [21], and none exists at 3 μm. This makes it crucial to accurately characterize its refractive index up to 3.14 μm, outside of the scope covered by literature data.

2. Tunable source design

2.1. Laser diode design

We propose a 1.55 μm source optimized for SPDC around 3.11 μm. This design results from back-and-forth optimizations between optical and electrical simulations, to jointly facilitate electron-hole injection, increase the conversion efficiency, and reduce losses. The conduction band and composition profile of this structure are shown in **Figure 1**. To compensate for the material dispersion, the laser diode is conceived so as to favor lasing on the TE_{20} mode (the second order in the direction of growth). To achieve this, the refractive index kept small in the center of the waveguide. As a consequence, the TE_{20} mode confinement inside the active area is stronger than for the TE_{00} mode. **Figure 2** shows the modes TE_{00} and TE_{20} supported by the waveguide at a wavelength of 1.55 μm. In order to achieve an efficient electron injection despite the conduction band increase in the core center, we reduce the series resistance with two strategies. Firstly, we introduce compositional gradients at the interfaces. Secondly, the waveguide core is only lightly doped. **Figure 3** depicts the conduction band and doping profile of the structure. An electrical simulation of this device using the software Nextnano yields a transparency current of 26 A/cm^2 at the transparency threshold.

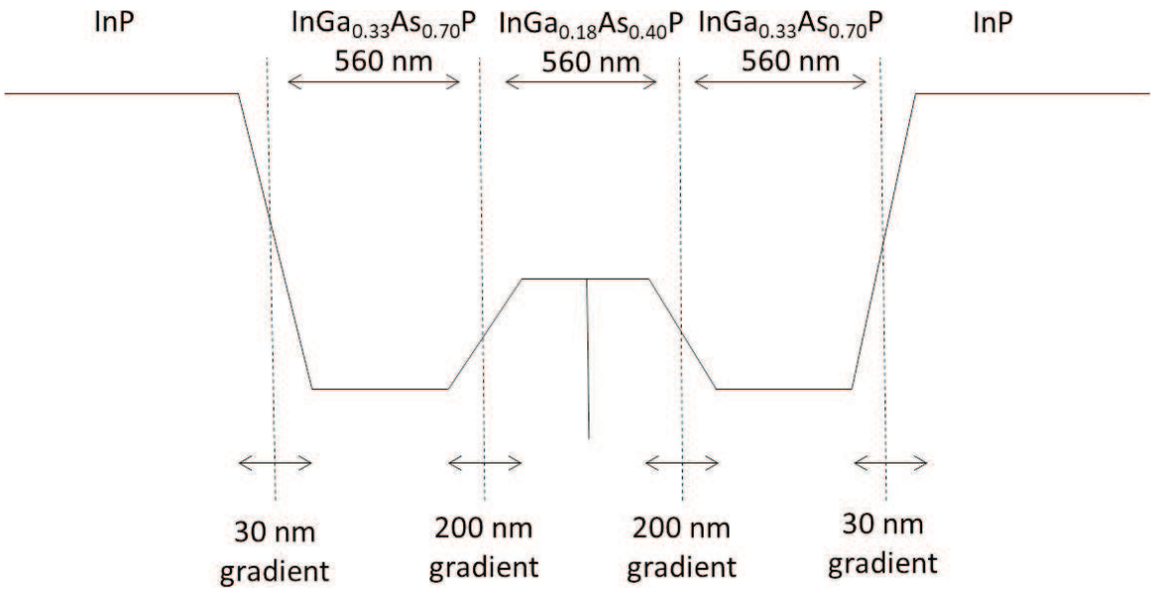

Figure 1. Conduction band and composition profile of the structure.

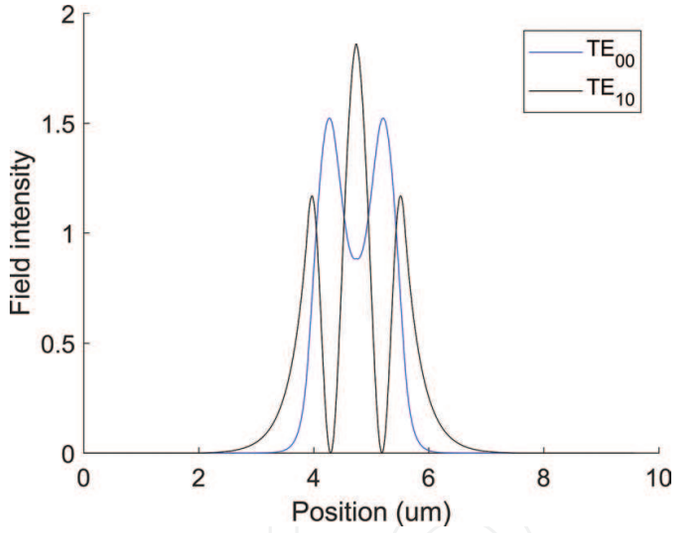

Figure 2. The first two even modes supported by the waveguide at $\lambda = 1.55$ μm.

2.2. Nonlinear properties

To achieve Type-II phase matching despite the error bars on the dispersion model and the fabrication tolerances, we use the ridge width as a crucial degree of freedom. **Figure 4** shows the phase mismatch at degeneracy vs. ridge width and pump wavelength, defined as

$$\Delta n = n\left(TE_{20}, 1.55\ \mu m\right) - \left[n\left(TE_{00}, 3.11\ \mu m\right) + n\left(TM_{00}, 3.11\ \mu m\right)\right]/2 \quad (1)$$

where the refractive indices are provided by our experimental data, presented in Part 2, and an interpolation of literature data [20]. By changing the ridge width from 3 to 7 μm, we are able to achieve phase matching for pump wavelengths of 1.50–1.60 μm. Furthermore, a variation in phase mismatch of ±0.02 can be compensated for by setting the correct ridge size. The

ridge width thus acts as a gross parameter to meet the phase-matching condition, which can be set after wafers have been grown and characterized.

During operation, temperature provides a supplementary degree of freedom to tune the pump wavelength and reach a wide range of frequencies. **Figure 5** shows the wavelengths

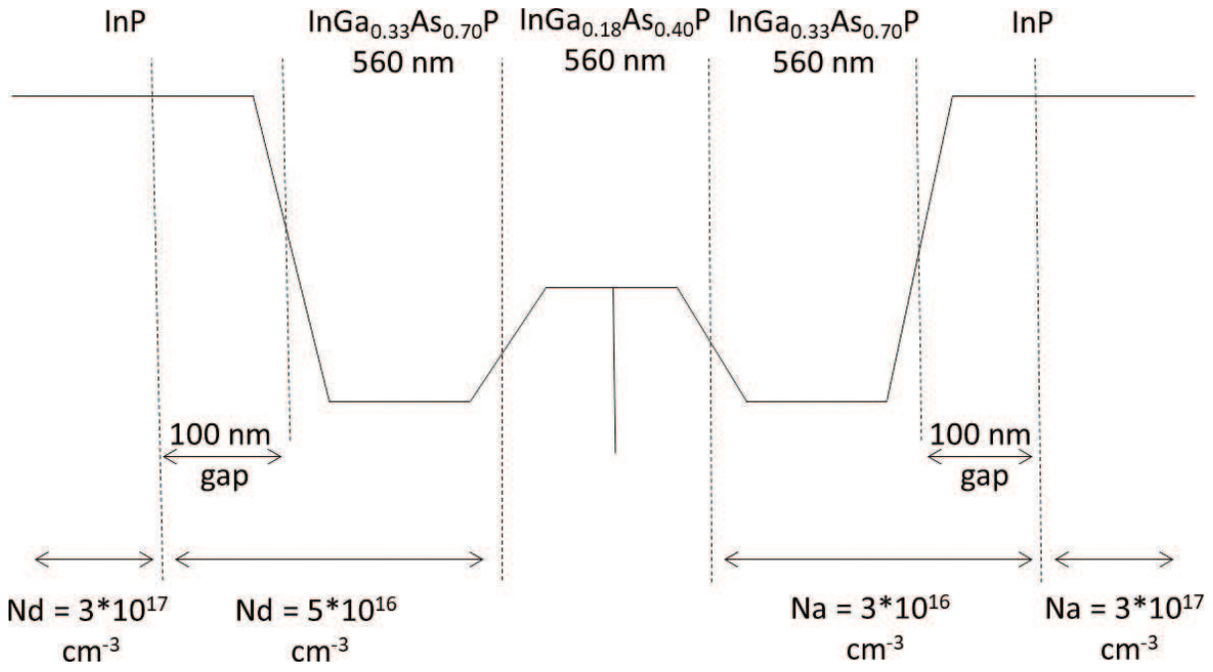

Figure 3. Conduction band and doping profile of the structure.

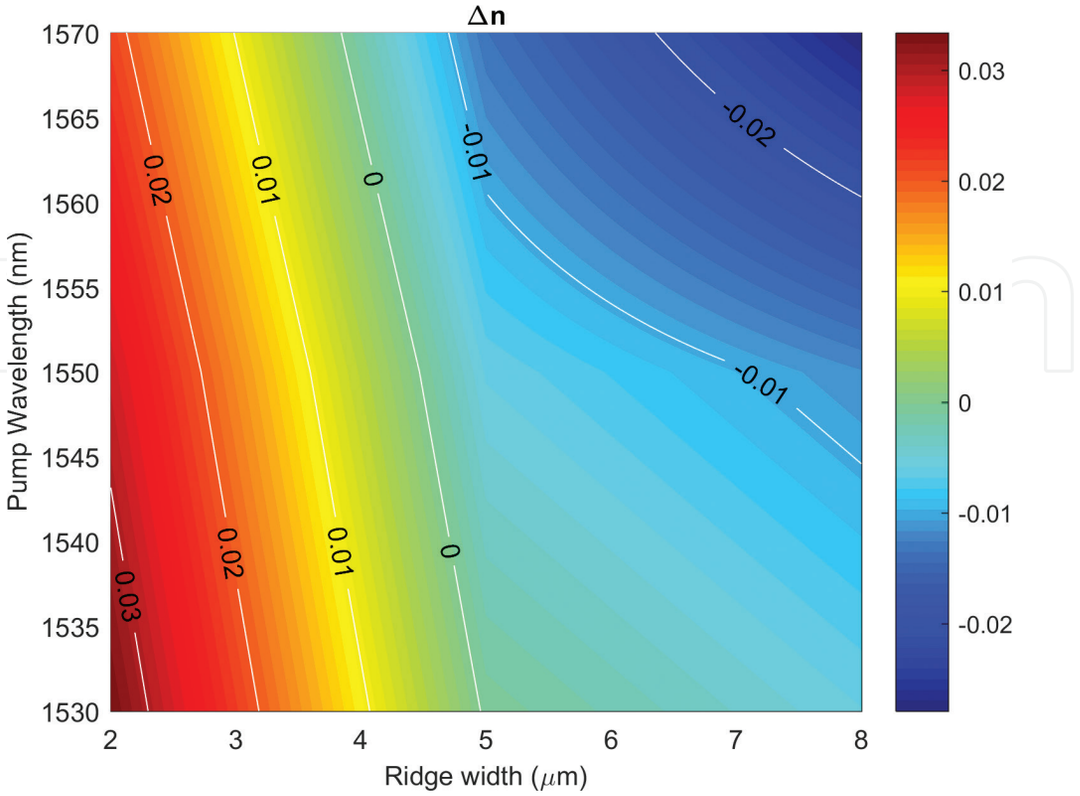

Figure 4. Phase mismatch in a deeply etched structure vs. ridge width and pump wavelength.

http://dx.doi.org/10.5772/intechopen.70753

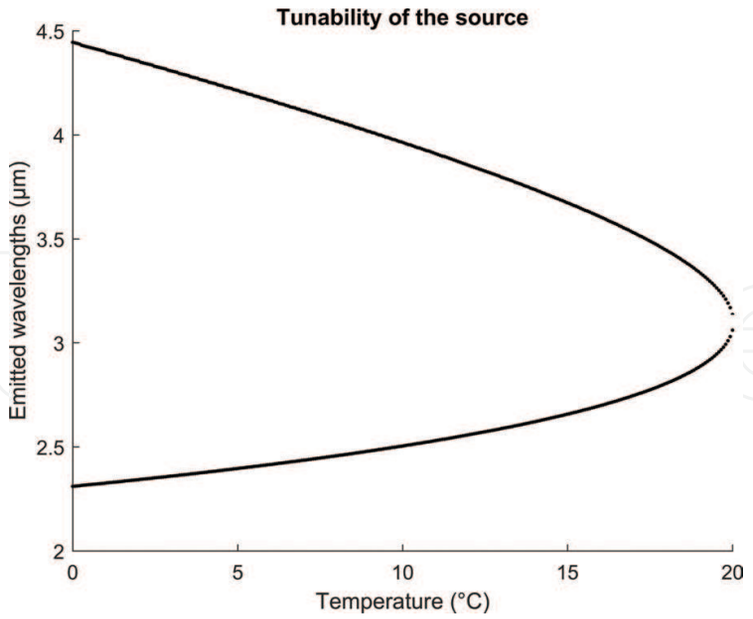

Figure 5. Emitted wavelengths for a device of ridge width 3.3 μm, emitting at 1.55 μm at 20°C.

of signal and idler emitted beams, for a source of ridge width 3.3 μm, emitting at a pump wavelength of 1.55 μm at 20°C. The dependency of quantum dots wavelength emission with temperature was assumed to be 0.5 nm/K from [22].

Figure 6 shows the profiles of the interacting modes, at a pump wavelength of 1.55 μm and signal and idler 3.11 μm. The expected conversion efficiency at a pump wavelength of 1.55 μm is 240% W^{-1} cm^{-2}. For an intracavity power of 100 mW, this corresponds to a parametric gain of 0.5 cm^{-1}. Since common InP QD lasers at 1.55 μm emit up to 20 mW outside the cavity without facet coatings [23], the above hypothesis on the intracavity power is very reasonable. The losses experimented by the mode at 3.11 μm are mainly expected to stem from free-carrier

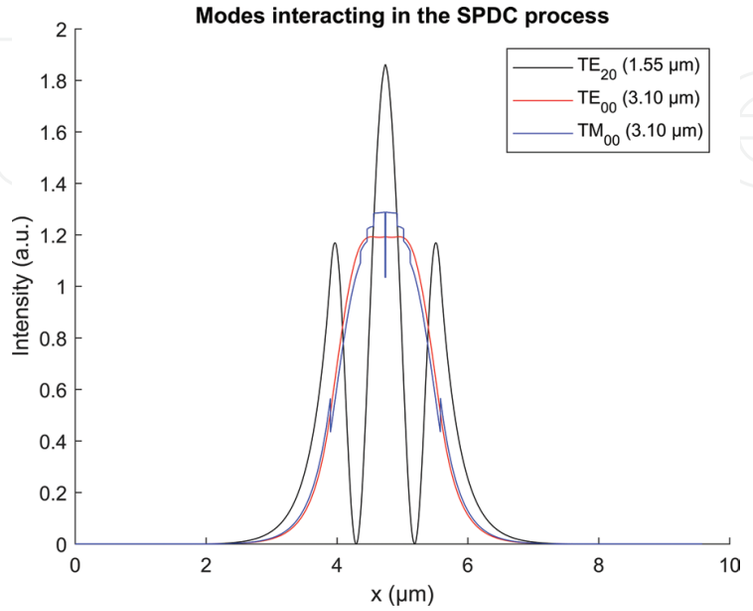

Figure 6. Field intensity of the three interacting modes in the SPDC process, at a pump wavelength of 1.55 μm.

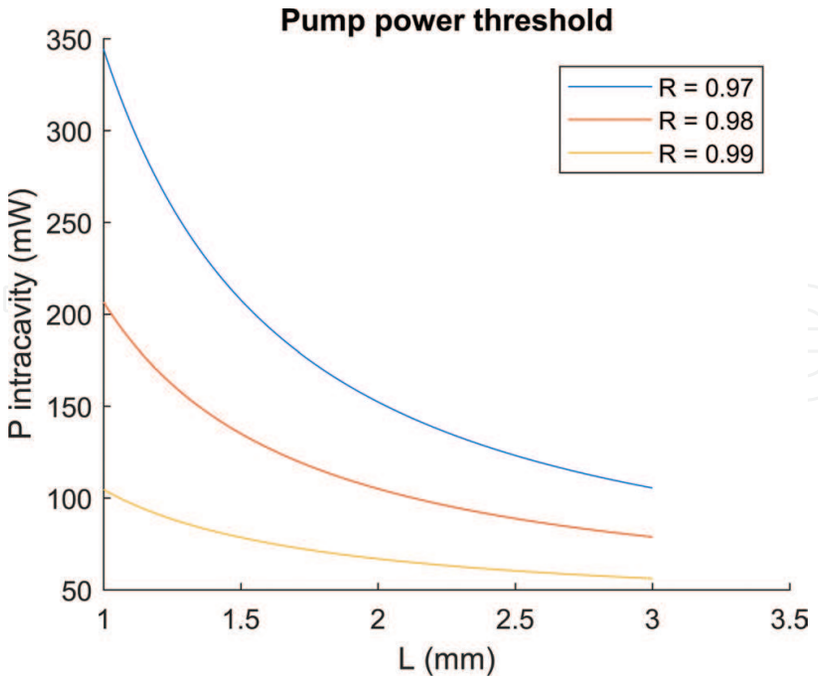

Figure 7. Intracavity pump power necessary for OPO threshold, vs. ridge length, for a few values of facet reflectivities.

absorption in doped layers, which we estimate at about 0.34 cm^{-1} for the TE_{00} mode. Reaching the OPO threshold in this device is therefore a challenging but achievable task, if mirror losses are minimized as in [13]. **Figure 7** shows the intracavity pump power necessary to reach oscillation for different mirror reflectivities and cavity lengths, assuming a conversion efficiency of 240%W^{-1} cm^{-2} and propagation losses of 0.34 cm^{-1}.

3. Index measurement

3.1. Principle

The evaluation of refractive indices was performed through an m-lines setup. This measurement relies on the determination of the coupling angle inside a slab waveguide of the material of interest. Our samples consist of a layer of $In_{1-x}Ga_xAs_yP_{1-y}$ lattice matched to InP grown over InP. As a result of the index contrast, the quaternary alloy acts as a planar waveguide. A diffraction grating was deposited or etched on the surface. The samples are mounted vertically on a rotating mount, and a laser is shone horizontally on the grating (**Figure 8**). Whenever the angle of light diffracted into the surface layer matches the bounce angle of a guided mode, coupling occurs. The guided light is collected by a detector placed at the exit facet of the sample. Coupling angles are given by the conservation of momentum

$$\left\|\vec{k}_{in}\right\| sin(\theta) = \left\|\vec{k}_{m}\right\| + m \left\|\vec{k}_{g}\right\| \quad (2)$$

where

$\left\|\vec{k}_{in}\right\|$ is the wave vector of the incident light, $\left\|\vec{k}_{m}\right\|$ is the wave vector of the mth guided mode, and $\left\|\vec{k}_{g}\right\|$ is the vector associated to the grating, of amplitude $2\pi/\Lambda$ (Λ being the period) and direction perpendicular to the grating lines, in the grating plane.

This equation leads to

$$N = sin(\theta) + m\,\lambda/\Lambda \tag{3}$$

where N is the effective index of the mth propagating mode. This measurement therefore estimates precisely the effective indices of the guided modes, as long as the period, wavelength, and coupling angles are known.

3.2. Sample fabrication

The planar structures were grown by molecular beam epitaxy and characterized by X-ray diffraction and photoluminescence prior to processing. An electronic resist with average thickness 70 nm was deposited on the surface (MAN2401 spin coated at 6000 rpm), and diffraction gratings were written by electronic lithography. The samples were then either used as such or very shallowly etched in a chemical solution before removing the resist. Both methods lead to shallow gratings on the guiding layer surface.

3.3. Optical setup

Three laser beams are combined with a precision of 0.01°: (1) a visible one (λ = 543 nm) for alignment and period measurements, (2) a tunable fibered laser around 1.55 μm, and (3) a free-space laser diode emitting at either 3.14 or 3.17 μm. The sample is placed on the axis of a rotating stage driven by a motor of step 0.001° and is precisely aligned so that the diffraction grating lines lie in the vertical direction (**Figure 9**). The light output at its exit facet is collected

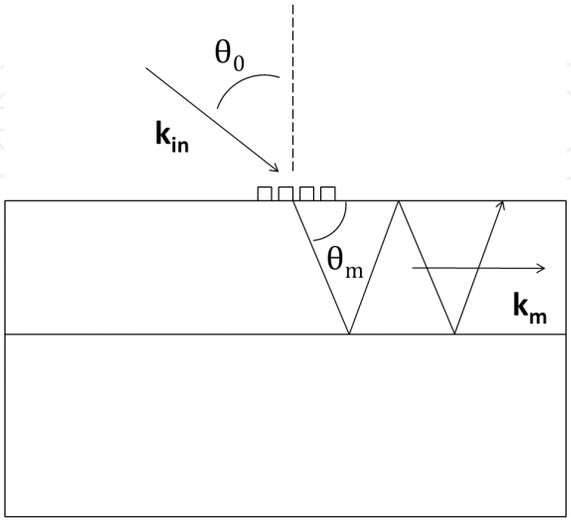

Figure 8. Coupling condition.

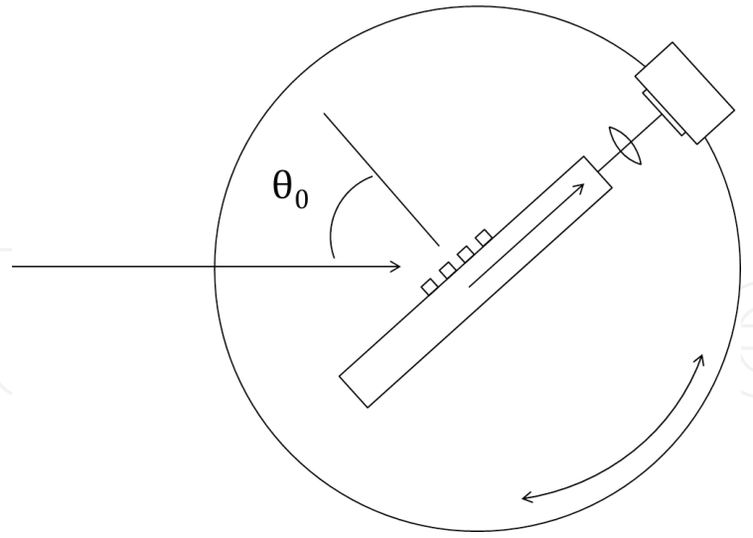

Figure 9. Optical setup for effective-index measurements.

with a detector placed after a slit (not shown here) and a focusing lens. All the detection setup is mounted on the stage, and it rotates rigidly with the sample. We used the same samples and gratings at 1.55 and 3 μm since the direction of the second-order diffracted beam at 1.55 μm roughly corresponds to the first order at 3.11 μm. To find the angle of normal incidence, measurements were done in a single long scan, with symmetric angles. Since all facets of a sample are cleaved and reflective, whenever θ_1 is a coupling angle, the light couples as well in the other direction for $\theta_2 = -\theta_1$ and reflects on the back facet, reaching the detector (**Figure 10**). Thus the angle of normal incidence was taken to be $(\theta_1 + \theta_2)/2$. This reduces the error bar due to a possible misalignment of the beams and to the motor backlash.

In order to determine the grating period, the visible laser was shone on the sample. Under the Littrow condition, the diffracted beam exits through the entrance slit and is collected through a beam splitter on a photodiode (**Figure 11**). The grating period is retrieved through the equality

$$2\,sin(\theta) = m\lambda/\Lambda \tag{4}$$

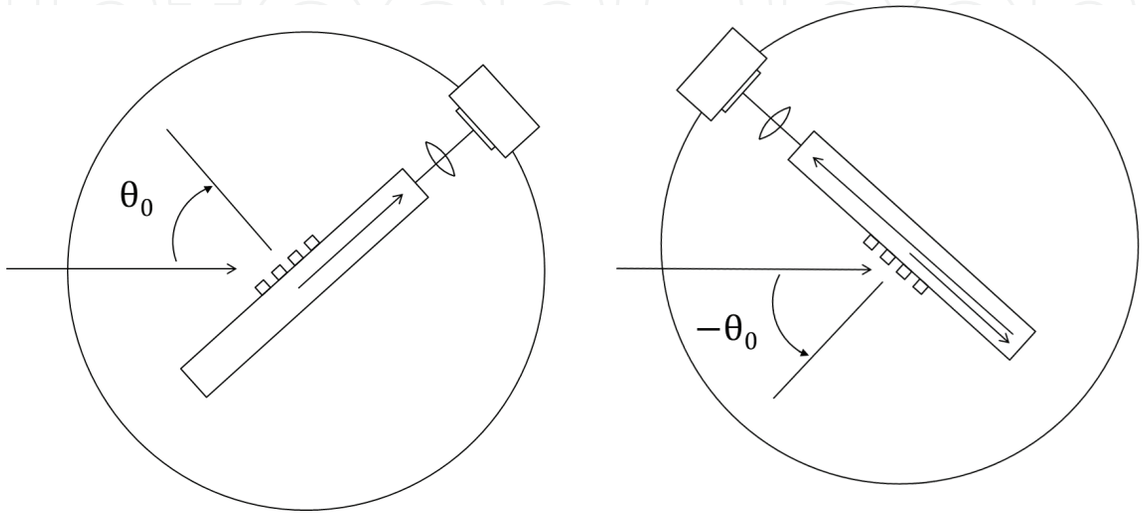

Figure 10. Determination of the angle of normal incidence.

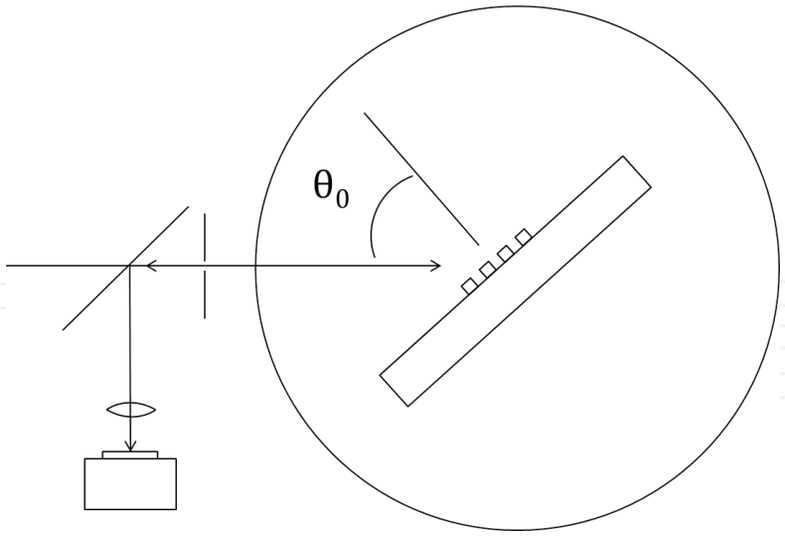

Figure 11. Optical setup for measuring the grating period.

3.4. Results

A typical result of coupling measurement is shown in **Figure 12**. The position of the peaks is determined with a precision of 0.01°. Since the effective indices are a function of material index and thickness of the guiding layer, each measured value corresponds to a range of possible {material index, thickness} pairs. This is represented in **Figure 13**, where one line corresponds to the space of parameters that minimize the difference between measured and theoretical indexes. Since more than one effective index is measured, it is possible to determine the right pair {material index, thickness}, at the crossing point. **Figure 14** shows the average difference between measured and effective indices. Waveguides support three modes at 1.55 μm, two at

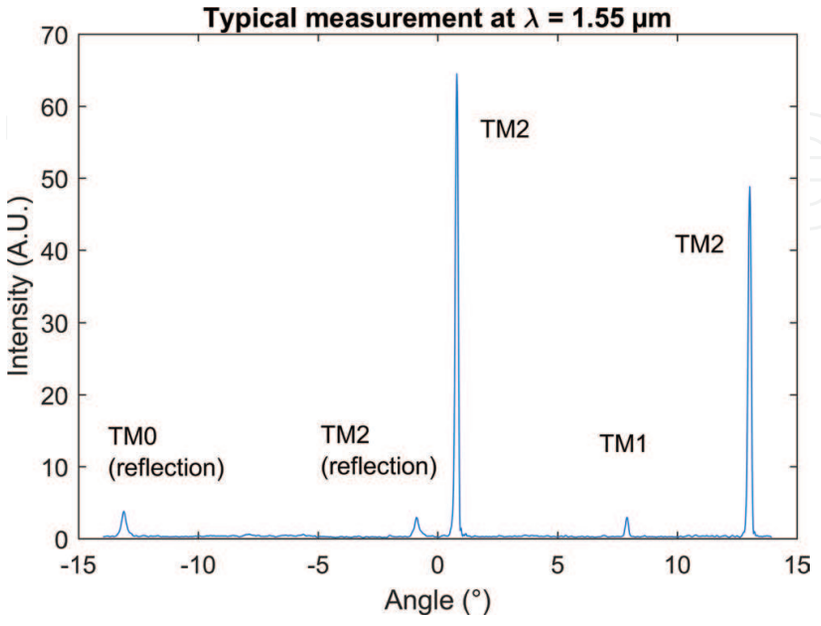

Figure 12. Determination of the refractive index and thickness for a slab of $In_{0.67}Ga_{0.33}As_{0.72}P_{0.28}$ at $\lambda = 1.55$ μm. Each line shows the possible range of data corresponding to the measured value of the effective index of a given waveguide mode.

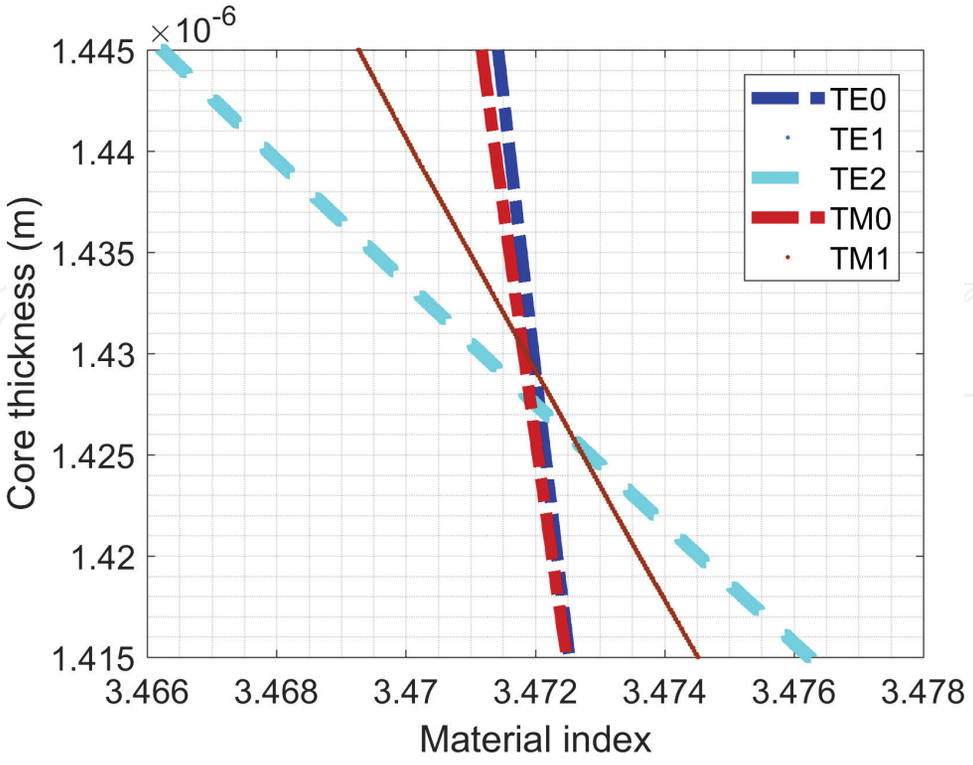

Figure 13. Coupling measurement into a slab of $In_{0.67}Ga_{0.33}As_{0.72}P_{0.28}$ on InP at a wavelength of 1.55 μm.

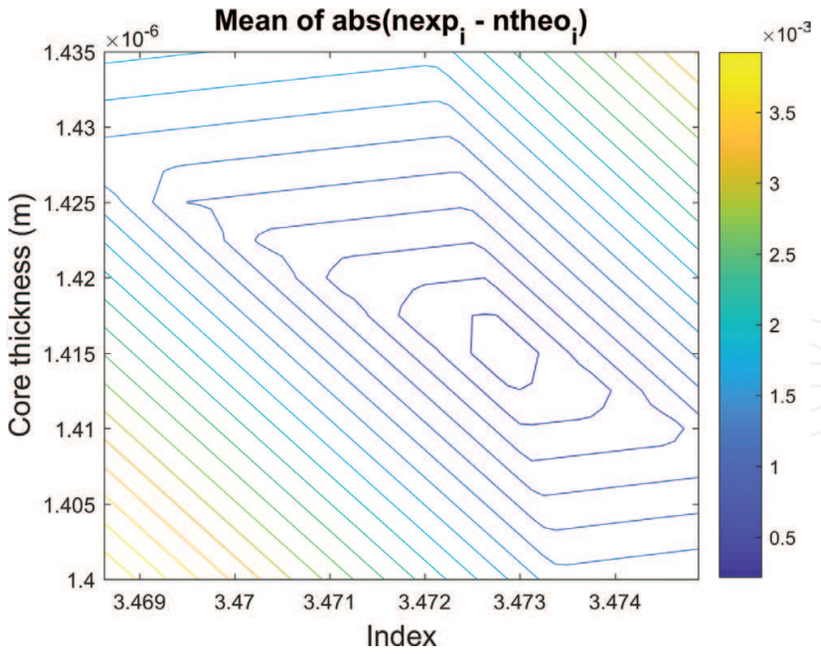

Figure 14. Determination of the refractive index and core thickness for a slab of $In_{0.67}Ga_{0.33}As_{0.72}P_{0.28}$ on InP at a wavelength of 1.55 μm. This figure shows the mean difference between calculated and measured effective indices. Area width gives an estimation of the error.

2.12 μm, and one at 3.14 μm. In order to derive the effective index at 3 μm, the guide thicknesses were estimated from the data at 1.55 μm (**Table 1**).

Figures 15–17 show the measured refractive indices as a function of As fraction, at wavelengths of 1.55, 2.12, and 3.14 μm. The data at 1.55 μm was compared to the model presented in [20]. At 2.12 and 3.14 μm, no model being available in the literature, we trace the data against a linear regression versus the molar fraction of As(y). The refractive index of InP from [24] was taken into account. **Figure 18** shows the refractive index versus wavelength, against a one-oscillator fit calculated from the Afromowitz model [25]. The fit parameters are presented in **Table 2**.

#	PL peak (μm)	da/a0	xGa	yAs	N (λ = 1.55 μm)	N (λ = 2.1 μm)	N (λ = 3.11 μm)
1	1.395	−0.0025	0.33	0.72	3.470		3.348
2	1.395	+0.002	0.33	0.72	3.472		3.349
3	1.395	n.m.	0.33	0.72		3.384	
4	1.346	n.m.	0.35	0.70	3.445		3.333
5	1.346	−0.0017	0.35	0.70	3.444		3.330
6	1.346	n.m.	0.35	0.70		3.370	
7	1.266	n.m.	0.24	0.55	3.391		3.289
8	1.266	+0.00078	0.24	0.55		3.325	

The lattice mismatch was measured by X-ray diffraction. Ga and As fraction are deduced through the model presented in [26].

Table 1. Physical properties and measured indices of the studied samples.

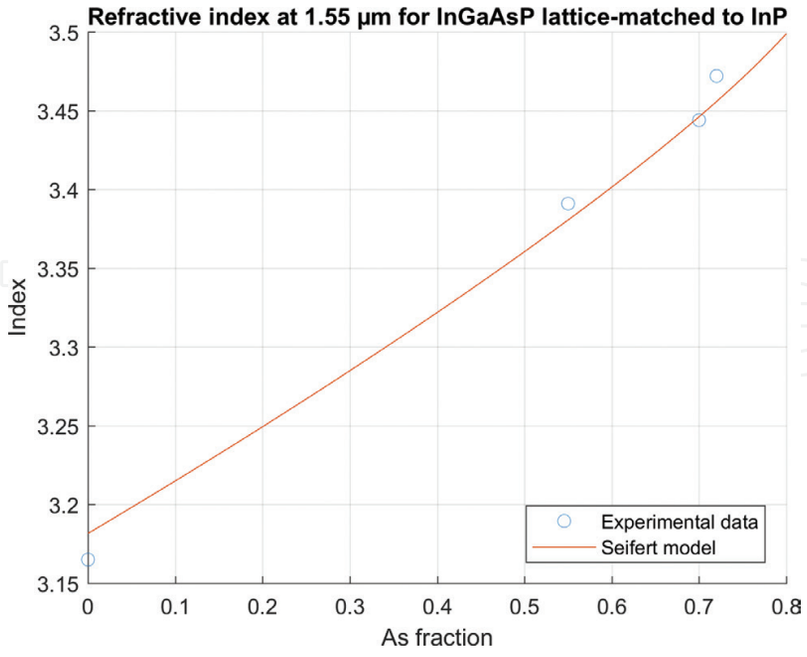

Figure 15. Refractive index measured at 1.55 μm vs. y, compared to [20].

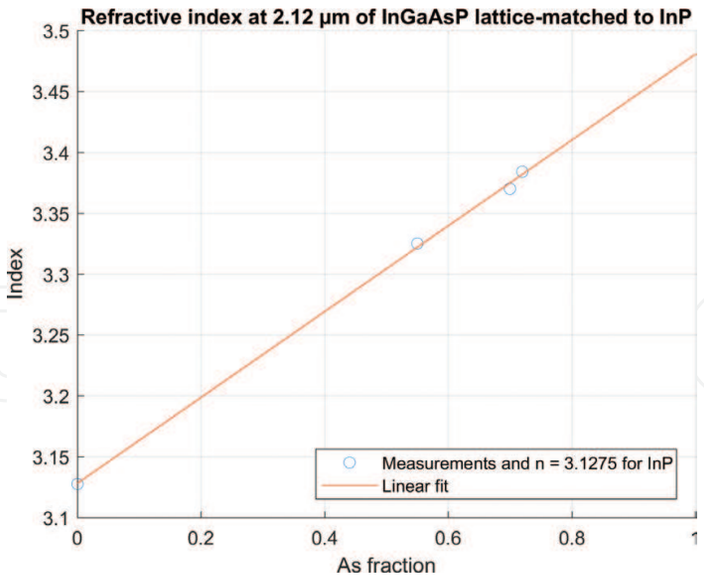

Figure 16. Refractive index measured at 2.12 µm vs. y (data plotted against a linear fit).

3.5. Discussion

The accuracy of this measurement is determined by several factors.

- Values of the grating period were determined by repeated measurements with a precision of 0.1 nm. This leads to a 0.3×10^{-3} error bar on the effective index.
- The uncertainty due to sample misalignment can be estimated at 0.5×10^{-3}. This may be explained by local variations of the resist filling factor and depth.
- In order to estimate the impact of the thin layer of photoresist on the effective indices, we performed a set of measurements on a sample covered with a thin photoresist grating. Then we etched it shallowly, removed the resist, and took a new set of data. The estimated thickness diminishes by 11 nm. This is in agreement with a profilometry of the etched grating depth, yielding 15 nm. The estimated core index is raised by 0.7×10^{-3}, a value lower than the possible variation of twice the experimental error. Thus we conclude that the resist has a negligible impact on the effective indices.
- While the laser beam alignment and position of the sample with respect to the rotating stage are adjusted in each measurement, one could point out that the axis of the rotating motor could be slightly misaligned with respect to the vertical axis and introduce a systematic error. A simple observation of the height of the beam reflection as the motor rotates indicates that the angle could be at most of 0.5 mrad. This leads, after a calculation, to an error on the effective index of 3×10^{-5}.
- Finally, incertitude on the composition is the most important. It is determined by the photoluminescence and lattice mismatch of the samples, with a precision of ~1%, through the model described in [26]. This corresponds to an uncertainty on the effective index of 4×10^{-3}. The deviation of our measurements with respect to literature and to a linear fit is in the range of 10^{-2} to 2×10^{-2}. This is in agreement with the observed variations of index due to the lattice mismatch observed in [16].

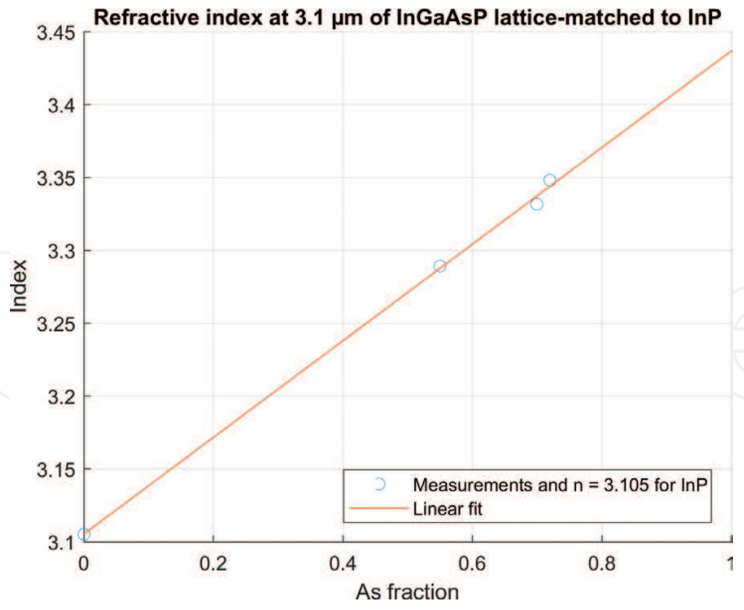

Figure 17. Refractive index measured at 3.14 μm vs. y (data plotted against a linear fit).

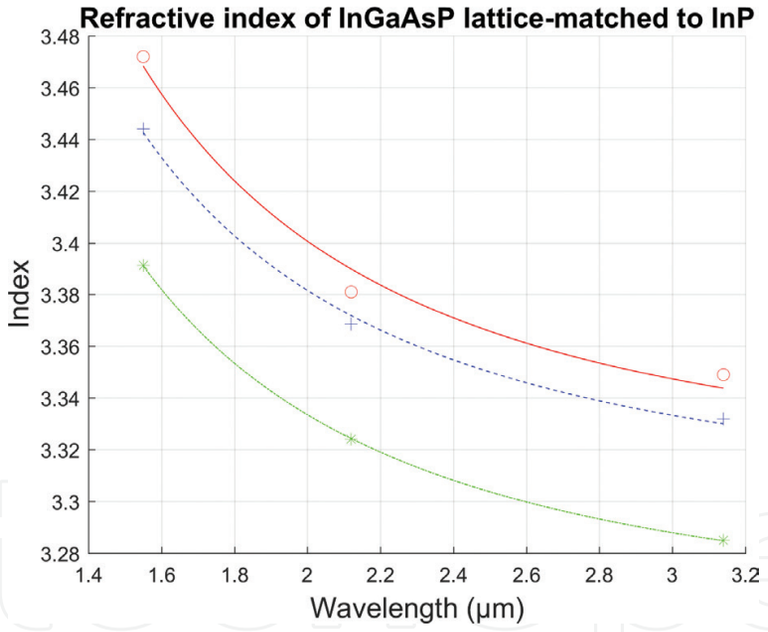

Figure 18. Refractive index of InGaAsP lattice matched to InP vs. wavelength for y = 0.72, 0.70, and 0.55. A one-oscillator fit (Afromowitz model) is added.

yAs	a	b
0.72	−0.0156	0.1007
0.70	−0.0144	0.1014
0.55	−0.0143	0.1044

Table 2. Parameters of the Afromowitz model inferred from the index measurements: a and b are extracted by a linear regression from $(n^2–1)^{-1} = a\,E^2 + b$, where E is the wavelength energy in eV.

Acknowledgements

This work is supported by a public grant overseen by the French National Research Agency (ANR) as part of the project DOPO. Authors thank the Commissariat à l'Energie Atomique and Direction Générale de l'Armement for PhD funding.

Author details

Alice Bernard[1,2], Marco Ravaro[1], Jean-Michel Gerard[2], Michel Krakowski[3], Olivier Parillaud[3], Bruno Gérard[3], Ivan Favero[1] and Giuseppe Leo[1*]

*Address all correspondence to: giuseppe.leo@univ-paris-diderot.fr

1 Laboratoire Matériaux et Phénomènes Quantiques, UMR 7162, Université Paris Diderot – CNRS, Paris, France

2 University Grenoble Alpes, CEA, INAC-PHELIQS, Grenoble, France

3 III-V Lab, Thales Research and Technology, Palaiseau, France

References

[1] Scholle K, Lamrini S, Koopmann P, Fuhrberg P. Bishnu Pal. 2 μm laser sources and their possible applications. In: Frontiers in Guided Wave Optics and Optoelectronics. InTech; 2010. ISBN 978-953-7619-82-4. February 1, 2010 under CC BY-NC-SA 3.0 license

[2] Siebenaler SP, Janka AM, Lyon D, Edlebeck JP, Nowlan AE. Methane detectors challenge: Low-cost continuous emissions monitoring. In: 2016 11th International Pipeline Conference 2016 Sep 26. American Society of Mechanical Engineers. New York, United States of America, ISBN : 978-0-7918-5027-5 pp. V003T04A013-V003T04A013

[3] Frish MB. Current and emerging laser sensors for greenhouse gas sensing and leak detection. In: Proceedings of the SPIE Sensing, Technologies & Applications Conference. Baltimore, MD, USA: Next Generation Spectroscopic Technologies VII; 21 May 2014. pp. 5-9

[4] Wang C, Sahay P. Breath analysis using laser spectroscopic techniques: Breath biomarkers, spectral fingerprints, and detection limits. Sensors. 2009 Oct 19;**9**(10):8230-8262

[5] Bandyopadhyay N, Bai Y, Tsao S, Nida S, Slivken S, Razeghi M. Room temperature continuous wave operation of $\lambda \sim$ 3-3.2 μm quantum cascade lasers. Applied Physics Letters. 2012 Dec 10;**101**(24):241110

[6] Devenson J, Barate D, Cathabard O, Teissier R, Baranov AN. Very short wavelength (λ = 3.1 – 3.3 μm) quantum cascade lasers. Applied Physics Letters. 2006 Nov 6;**89**(19): 191115

[7] Gaimard Q, Cerutti L, Teissier R, Vicet A. Distributed feedback GaSb based laser diodes with buried grating. Applied Physics Letters. 2014 Apr 21;**104**(16):161111

[8] Dong L, Li C, Sanchez NP, Gluszek AK, Griffin RJ, Tittel FK. Compact, low power consumption methane sensor based on a novel miniature multipass gas cell and a CW, room temperature interband cascade laser emitting at 3.3 μm. In: SPIE OPTO 2016 Feb 13. International Society for Optics and Photonics. Bellingham, Washington USA. pp. 97550I-97550I

[9] Manfred KM, Ritchie GA, Lang N, Röpcke J, van Helden JH. Optical feedback cavity-enhanced absorption spectroscopy with a 3.24 μm interband cascade laser. Applied Physics Letters. 2015 Jun 1;**106**(22):221106.

[10] Ren W, Luo L, Tittel FK. Sensitive detection of formaldehyde using an interband cascade laser near 3.6 μm. Sensors and Actuators B: Chemical. 2015 Dec 31;**221**:1062-1068

[11] Sohler W, Hu H, Ricken R, Quiring V, Vannahme C, Herrmann H, Büchter D, Reza S, Grundkötter W, Orlov S, Suche H. Integrated optical devices in lithium niobate. Optics and Photonics News. 2008 Jan 1;**19**(1):24-31

[12] Pomarico E, Sanguinetti B, Gisin N, Thew R, Zbinden H, Schreiber G, Thomas A, Sohler W. Waveguide-based OPO source of entangled photon pairs. New Journal of Physics. 2009 Nov 24;**11**(11):113042

[13] Savanier M, Ozanam C, Lanco L, Lafosse X, Andronico A, Favero I, Ducci S, Leo G. Near-infrared optical parametric oscillator in a III-V semiconductor waveguide. Applied Physics Letters. 2013 Dec 23;**103**(26):261105

[14] Moore SA, O'Faolain L, Cataluna MA, Flynn MB, Kotlyar MV, Krauss TF. Reduced surface sidewall recombination and diffusion in quantum-dot lasers. IEEE Photonics Technology Letters. 2006 Sep;**18**(17):1861-1863

[15] Barbarin Y, Anantathanasarn S, Bente EA, Oei YS, Smit MK, Notzel R. 1.55 μm range InAs–InP (100) quantum-dot Fabry–Pérot and ring lasers using narrow deeply etched ridge waveguides. IEEE Photonics Technology Letters. 2006 Dec 15;**18**(24):2644-2646

[16] Broberg B, Lindgren S. Refractive index of $In_{1-x}Ga_xAs_yP_{1-y}$ layers and InP in the transparent wavelength region. Journal of Applied Physics. 1 May 1984;**55**(9):3376-3381

[17] Amiotti M, Landgren G. Ellipsometric determination of thickness and refractive index at 1.3, 1.55, and 1.7 μm for $In_{1-x}Ga_xAs_yP_{1-y}$ films on InP. Journal of Applied Physics. 1993 Mar 15;**73**(6):2965-2971

[18] Henry C, Johnson L, Logan R, Clarke D. Determination of the refractive index of InGaAsP epitaxial layers by mode line luminescence spectroscopy. IEEE Journal of Quantum Electronics. 1985 Dec;**21**(12):1887-1892

[19] Fiedler F, Schlachetzki A. Optical parameters of InP-based waveguides. Solid State Electronics. 1987 Jan 31;**30**(1):73-83

[20] Seifert S, Runge P. Revised refractive index and absorption of $In_{1-x}Ga_xAs_yP_{1-y}$ lattice-matched to InP in transparent and absorption IR-region. Optical Materials Express. 2016 Feb 1;**6**(2):629-639

[21] Chandra P, Coldren LA, Strege KE. Refractive index data from $In_{1-x}Ga_xAs_yP_{1-y}$ films. Electronics Letters. 1981 Jan 8;**17**(1):6-7

[22] Landin L, Borgström M, Kleverman M, Pistol ME, Samuelson L, Seifert W, Zhang XH. Optical investigation of In:As/InP quantum dots at different temperatures and under electric field. Thin Solid Films. 2000 Mar 27;**364**(1):161-164

[23] Reithmaier JP, Eisenstein G, Forchel A. InAs/InP quantum-dash lasers and amplifiers. Proceedings of the IEEE. 2007 Sep;**95**(9):1779-1790

[24] Pettit GD, Turner WJ. Refractive index of InP. Journal of Applied Physics. 1965 Jun 1; **36**(6):2081

[25] Afromowitz MA. Refractive index of $Ga_{1-x}Al_xAs$. Solid State Communications. 1974 Jul 1;**15**(1):59-63

[26] Kuphal E. Phase diagrams of InGaAsP, InGaAs and InP lattice-matched to (100) InP. Journal of Crystal Growth. 1984 Aug 1;**67**(3):441-457